metals

MDPI

Article

Tempering Behavior of Novel Low-Alloy High-Strength Steel

Valeriy Dudko [1,2], Diana Yuzbekova [1,2], Sergey Gaidar [1], Sofia Vetrova [1] and Rustam Kaibyshev [1,*]

[1] Russian State Agrarian University-Moscow Timiryazev Agricultural Academy, 127550 Moscow, Russia
[2] Laboratory of Mechanical Properties of Nanostructured Materials and Superalloys, Belgorod State National Research University, 308015 Belgorod, Russia
* Correspondence: kajbyshev@rgau-msha.ru

Abstract: The effect of tempering on the mechanical properties, structure, and dispersion of secondary phase particles is studied in 0.4%C-2%Si-1%Cr-1%Mo-VNb steel. This steel austenitized at 900 °C with subsequent water quenching exhibits a yield stress of 1445 MPa and a lath martensite structure with MX particles of ~40 nm located in matrix and boundary M_6C carbides of ~210 nm. Tempering in the temperature interval of 200–400 °C provides a yield stress of 1625 MPa due to the precipitation of ε-carbide and cementite within laths. The yield stress decreases to 1415 and 1310 MPa after tempering at 500 and 650 °C, respectively, due to the replacement of matrix carbides by boundary $M_{23}C_6$ carbide. A Charpy V-notch impact energy of ~12 J/cm^2 is almost independent from tempering temperatures of up to 400 °C and increases up to ~33 J/cm^2 after tempering at 650 °C due to decreased yield stresses and increased plasticity.

Keywords: ultrahigh-strength low-alloy steels; tempering behavior; precipitation sequence

Citation: Dudko, V.; Yuzbekova, D.; Gaidar, S.; Vetrova, S.; Kaibyshev, R. Tempering Behavior of Novel Low-Alloy High-Strength Steel. *Metals* **2022**, *12*, 2177. https://doi.org/10.3390/met12122177

Academic Editors: Andrii Kostryzhev and Zhinan Yang

Received: 12 November 2022
Accepted: 14 December 2022
Published: 17 December 2022

Publisher's Note: MDPI stays neutral with regard to jurisdictional claims in published maps and institutional affiliations.

1. Introduction

Ultrahigh-strength low-alloy steels (UHSSs) with yield stresses (YSs) >1400 MPa were successfully employed about 70 years ago [1]. The high strength of these medium-carbon steels containing various amounts of chromium, molybdenum, nickel, silicon, and vanadium is achieved by heat treatment consisting of austenitizing followed by water quenching with subsequent low-temperature tempering [1–3]. This form of processing results in hierarchical lath martensite structures [4] and a dispersion of nanosized carbides [1,5–7]. Satisfactory fracture toughness is provided by metallurgical control [1–3]. The yield stress (YS) of these steels could be increased by dispersion strengthening via additional alloying by using carbide-forming elements such as Nb [5–7]. MX carbonitrides may enhance YS without a loss of fracture toughness [5,7].

A novel steel 0.4%C-1.6%Si-1%Cr-0.95%Mo with V and Nb additions was recently developed as a UHSS. This steel contains low quantities of phosphorus and sulfur to avoid embrittlement [1–3,6]. Carbon provides interstitial solution strengthening for lath martensite structures and the formation of a high volume fraction of carbides and carbonitrides under tempering [5,6]. Silicon and Mo contribute to substitutional solid solution strengthening [5–7]. Silicon restricts the growth of carbides and delays the decomposition of martensite during tempering processes [6,8,9]. Cr and Mo are partially retained in ferrite after the decomposition of martensite after tempering at $T \geq 600$ °C and slow down diffusional processes [10]. As a result, a combination of substitutional elements provides sufficient hardenability of this steel. In addition, Mo suppresses temper embrittlement and provides solid solution strengthening [5,10]. The other portion of these elements forms nano-sized carbides [5,7]. Microalloying by Nb and V is performed in order to produce a dispersion of MX carbonitrides that exert the dispersion strengthening effects [5,7,11]. Nanoscale Nb(C,N) carbonitrides prevent the growth of prior austenite grains (PAG) [4] during austenitizing. The small size of PAGs refines packets and blocks that may increase YS [12,13].

Studies focusing on the tempering behavior of low-alloy UHSS are limited [5,14–16]. The goal of the present work is to examine the tempering behavior of the 0.4%C-1.6%Si-1%Cr-0.95%Mo with V and Nb additions. The effect of tempering on the mechanical properties, structure, and dispersion of secondary phase particles is considered. Specific attention is given to phase transformations occurring during tempering.

2. Materials and Methods

A steel with a chemical composition of Fe-0.43C-1.60Si-0.01Mn-1.1Cr-0.95Mo-0.08V-0.05Nb-0.04Ti-0.003B-0.007S-0.004P, all in wt.%, was examined. This steel was austenitized at a temperature of 900 °C for 40 min followed by water quenching. Next, the specimens were tempered for 1 h at temperatures of 200, 280, 400, 500, 600, and 650 °C.

The Rockwell hardness tests were conducted using a Wolpert Wilson hardness tester 600 MRD (Illinois ToolWorks Inc., Norwood, MA, USA). The tensile tests were carried out at room temperature using flat specimens with a cross-sectional area of 7×3 mm^2 and a 35 mm gauge length and Instron 5882 testing machine (Illinois ToolWorks Inc., Norwood, MA, USA). Standard Charpy V-notch specimens were tested at room temperature using the Instron SI-1M impact machine with a maximum energy of 450 J with the Instron Dynatup Impulse data acquisition system (Instron corporation, Grove City, PA, USA) following the ASTM E-23 standard [17].

Structural characterizations after different quenching and tempering were carried out using a JEM-2100 transmission electron microscope (TEM) (JEOL Ltd., Tokyo, Japan) and a Quanta 600 FEG scanning electron microscope (FEI Corporation, Hillsboro, OR, USA) incorporating an orientation imaging microscopy (OIM) system. TEM foils were prepared by double-jet electropolishing using a solution of 10% perchloric acid in glacial acetic acid. Extraction replicas were prepared by etching the polished surface of the specimen in a solution of 97% H_2O, 2% HNO_3, and 1% HF followed by the evaporation of carbon onto a polished and etched surface. Then, the metallic matrix was dissolved in 10% HCl with ethanol at a voltage of 17 V. The small squares of carbon extraction replicas were captured using nickel grids. The transverse lath sizes were measured from TEM micrographs by the linear intercept method, including all clearly visible sub-boundaries. At least 40 particles of each type of precipitate were analyzed in order to measure average size. The dislocation densities were evaluated by counting individual dislocations in the grain/subgrain interiors, and each data point represents at least six arbitrarily selected representative TEM images that were obtained using two-beam conditions with {002} or {013} scattering planes and a small positive deviation parameter.

The reconstruction of PAGs was conducted in accordance with the method suggested by Gey and Humbert [18,19]. This method assumes that the orientation variants inherited from the same PAGs are characterized by very specific misorientations [4], and the grain boundaries between these variants can be readily distinguished from other boundaries in an EBSD map. The remaining boundaries are believed to separate the martensite variants from the different PAGs, i.e., they represent the boundaries of these grains. Other details of mechanical and structural characterization are described in previous works [5,20,21].

The equilibrium mass fractions and Gibbs energies of the precipitated phases were calculated by the Thermo-Calc software (Ver. 5, Thermo-Calc Software, Stockholm, Sweden) using the TCFE7 database.

Differential scanning calorimetry (DSC) was performed using an SDT Q600 (TA Instruments New Castle, DE, USA) calorimeter. The mass of samples was ~142 mg, and a protective atmosphere of pure argon was used. Samples austenitized at a temperature of 900 °C and finally water-quenched were heated from 20 to 550 °C at a rate of 10 °C/min.

3. Results and Discussion

3.1. Thermodynamic Analysis

The effect of temperatures, ranging from 200 to 1200 °C, on the phase equilibrium is shown in Figure 1. The Gibbs energy of M_3C carbides decreases by 23 times when the

temperature increases from 280 to 500 °C (Figure 1b). As a result, the fraction of cementite increases by a factor of ~10 (Figure 1a) and the ratio of Fe/Cr in cementite decreases from ~57 to ~7 (Figure 1c). It should be noted that the TCFE7 database of Thermo-Calc software contains no ε-carbide and only a prediction of more stable M_3C precipitation is possible. $M_{23}C_6$ carbides are more stable than M_3C carbides at 500 °C because the Gibbs energy of the former is lower by a factor of ~2.4 (Figure 1b). With increasing temperature toward 650 °C, the Gibbs energies of these two phases conform with one another. In accordance with the calculations, $M_{23}C_6$ carbides start to precipitate at 500 °C and coexist with M_3C up to 700 °C (Figure 1a). It is worth noting that $M_{23}C_6$ carbides contain a very high portion of Fe atoms, and the ratio of Fe/∑(Cr + Mo) is ~2.4 (Figure 1e).

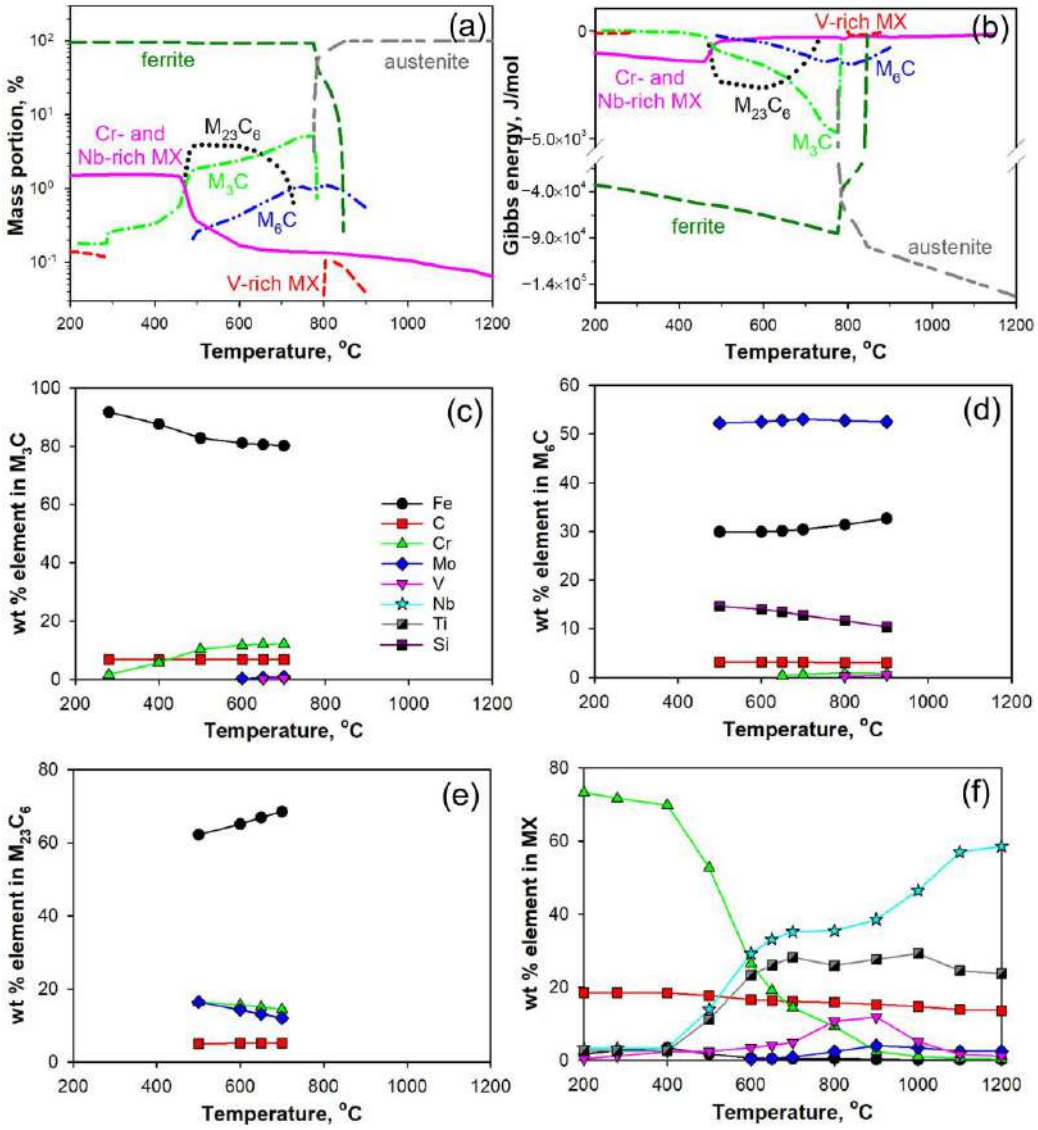

Figure 1. Equilibrium phase diagram of the studied steel: phase fractions (**a**), Gibbs energies (**b**), and the chemical compositions of M_3C (**c**), M_6C (**d**), $M_{23}C_6$ (**e**), and MX (**f**) phases.

Another phase predicted by Thermo-Calc is M_6C carbides that precipitate at temperatures from 500 °C to 900 °C. The Gibbs energies for this phase decrease up to a temperature of 800 °C (Figure 1b). The precipitates are predicted to be enriched by Si and Mo with a ratio of Fe/∑(Si + Mo) ~ 0.45 (Figure 1d).

Thermodynamic calculations predict two phase separations of carbonitrides relative to V-rich MX and MX enriched by Cr and Nb. (Figure 1a). The first type of carbonitride is enriched with V and precipitates in temperature regions ranging from 200 to 280 °C

and from 800 to 900 °C. The second type of carbonitride is enriched by Cr, Nb, and Ti and precipitates in a wide temperature interval ranging from 200 to 1200 °C. The atoms of Cr are replaced by Nb with increasing temperatures (Figure 1f). The Gibbs energies of MX carbonitrides with Cr, Nb, and Ti are high and reach up to 400 °C and then sharply decrease. At a temperature of 500 °C, this process is accompanied by a replacement of Cr by Nb in their chemical compositions (Figure 1b,f).

Therefore, in the 0.4%C-1.6%Si-1%Cr-0.95%Mo steel with V and Nb, the following precipitation sequences in the martensite take place in accordance with Thermo-Calc calculations at temperatures from 200 to 467 °C:

$$\text{Martencite} \rightarrow M_3C + MX$$

and at temperatures from 467 to 741 °C:

$$\text{Martencite} \rightarrow M_3C + M_{23}C_6 + M_6C + MX.$$

3.2. DSC Analysis

Figure 2 shows the DSC curve. The weak exothermic peak is distinguished at 200 °C and may be attributed to carbon clustering, retaining the austenite transformation into ferrite or precipitation of ε-carbides [22]. The large exothermic peak with a maximum at a temperature of 280 °C can be distinguished between temperatures of 220 and 420 °C. In accordance with Thermo-Calc calculations, cementite and MX carbonitrides could precipitate in this temperature range. However, Thermo-Calc predicts equilibrium phases and the literature data show that metastable carbides such as ε-carbides could precipitate at temperatures between 220 and 420 °C instead of cementite [7,22]. The small weak exothermic peak at 380 °C within the large peak could be attributed to the precipitation of cementite and the presence of a strong exothermic peak at 467 °C could be associated with the precipitation of $M_{23}C_6$ carbide or cementite. It seems that the endothermic reaction between 390 and 420 °C is attributed with the dissolution of ε-carbide. The additions of Si, Mo, and Cr may increase the precipitation temperatures of ε-carbide and cementite by 100 °C in comparison with typical high-carbon and low-alloy steels [9,22]. The additions of Cr and Mo provide precipitation of $M_{23}C_6$ carbides and the dissolution of cementite.

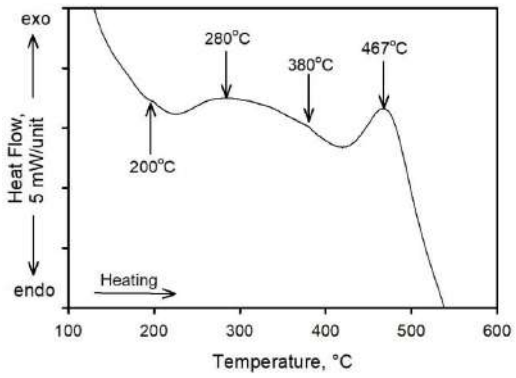

Figure 2. DSC curves of 0.4%C-1.6%Si-1%Cr-0.95%Mo steel with V and Nb obtained at 10 °C/min. The arrows indicate the onset of a reaction and peak temperatures.

3.3. Mechanical Properties

The typical engineering-stress–engineering-strain and true-stress–true-strain curves obtained by tensile tests are shown in Figure 3. The values of yield stress (YS), S_y; ultimate tensile strength (UTS), S_u; uniform elongation, El_u; total elongation, El_t; Rockwell hardness, *HRC* are summarized in Table 1. Continuous yielding [7,23] is observed after all tempering conditions. However, an increase in tempering temperature leads to a decrease in strain hardening. The onset of strain hardening occurs soon after yielding; the strain-hardening stage extends with increasing tempering temperature and the onset of necking shifts relative

to higher strains. Tempering at 200 °C leads to an increase in YS by 180 MPa as compared with the quenched specimens. In the temperature range of 200–400 °C, the YS of 1625 MPa remains unchanged, while UTS and El_u values decrease slowly with increasing temperature (Figure 3a, Table 1). As a result, hardness also decreases insignificantly.

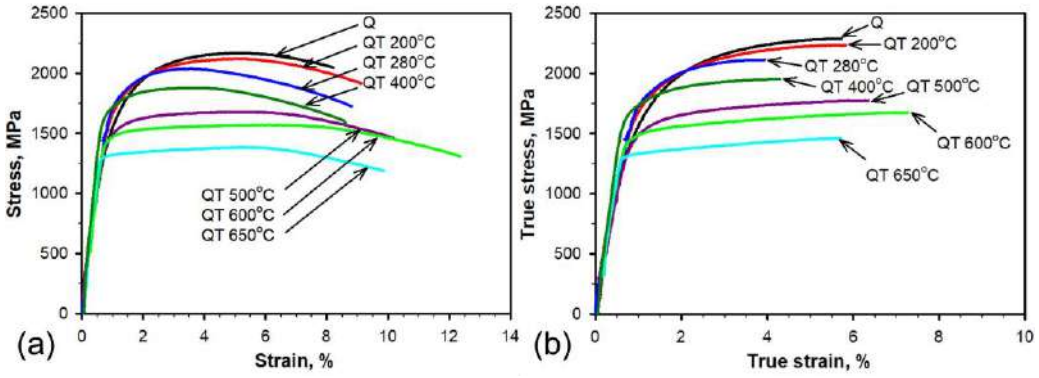

Figure 3. Engineering curves (**a**) and true-stress–true-strain curves (**b**) at room temperature of the 0.4%C-1.6%Si-1%Cr-0.95%Mo steel with V and Nb after quenching (Q) and different tempering (T) temperatures.

Table 1. Mechanical properties of 0.4%C-1.6%Si-1%Cr-0.95%Mo steel with V and Nb after quenching from 900 °C into water and tempering at different temperatures.

Tempering Temperature, °C	S_y, MPa	S_u, MPa	El_u, %	El_t, %	*HRC*	*CVN*, J/cm^2
20	1445	2170	4.9	7.2	55	10
200	1625	2120	4.7	8.2	54	12
280	1695	2040	3.4	8.0	54	14
400	1675	1880	3.6	8.0	53	12
500	1415	1680	5.0	10.2	50	21
600	1460	1580	6.5	11.5	48	26
650	1310	1390	5.0	9.2	44	33

The high value of YS may indicate that the parameters of microstructures such as lath sizes and dislocation densities are stable when tempering at 200–400 °C. Obviously, the decrease in the solid solution strengthening process balances the increase in the dispersion strengthening process due to the precipitation of ε-carbide and M_3C carbides at temperatures of 280–400 °C. Moreover, precipitation strengthening results in the increase in YS, which reaches a maximum value after tempering at 280 °C. However, the depletion of solid solution by carbon because of the carbides precipitation reduces the UTS of the steel and the precipitation of M_3C decreases the El_u values. An increase in tempering temperatures up to 600 °C leads to a further decomposition of martensite and a considerable decrease in YS by ~230 MPa and UTS by ~360 MPa, and an insignificant increase in ductility is observed.

The Rockwell hardness of the steel gradually decreases from 55 to 48 HRC while the tempering temperatures increase from 200 to 600 °C. At tempering temperatures of 650 °C, YS and UTS decrease below 1400 MPa. The strain-hardening processes decrease with increasing tempering temperatures and the ductility remains low after tempering at 650 °C (Figure 3b). Therefore, the ductility of this steel cannot be improved by tempering at relatively high temperatures.

The load–deflection curves from instrumental Charpy impact tests are presented in Figure 4, and Charpy impact fracture energies, CVN, are indicated in Table 1. A Charpy V-notch impact energy of ~12 J scarcely changes with the increase in tempering temperatures from 200 to 400 °C (Table 1). At T ≥ 500 °C, increasing the temperature leads to a gradual increase in the Charpy impact energy (Table 1). However, even after tempering at 650 °C,

the Charpy V-notch impact energy of ~33 J/cm^2 is relatively low. It is worth noting that the values of impact toughness are typical for UHSS with a low-temperature-tempered martensite structure [1]. A significant increase in the impact toughness of these steels could be attained by the tempforming process only [24,25].

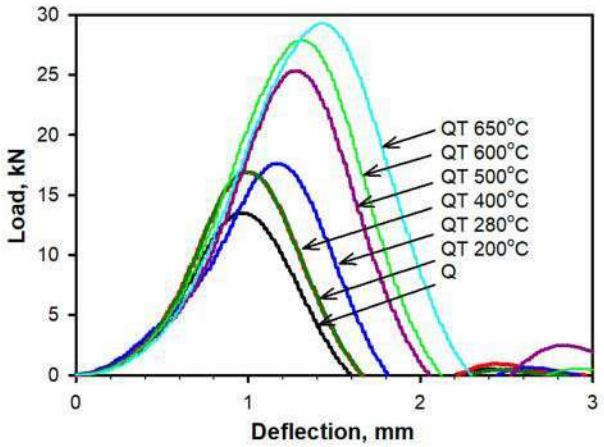

Figure 4. Load vs. deflection dependencies at room temperatures of the 0.4%C-1.6%Si-1%Cr-0.95%Mo steel with V and Nb after quenching (Q) and different tempering (T) temperatures.

Usually, the general yield load is determined from the flat portion in the load–deflection-recorded curve of the Charpy V-notch test. High-strength steels often contain no flat portions in their curves [26]. The minimal value of the general yield load (P_{GY}) can be estimated from slip-line fields solutions for V-notch Charpy specimens [26,27], which gives

$$P_{GY} = 2C_f S_y B(W - a)^2/\beta/L,$$

where L denotes the span (=40 mm); W denotes the specimen width (=10 mm); B denotes the specimen thickness (=10 mm); a denotes the notch depth (=2 mm); C_f = 1.363 denotes the constraint factor for ASTM tup; β = 2 denotes the Tresca yield criterion. The calculated values of P_{GY} and maximum loads in load–deflection curves from Figure 4 are collected in Table 2. At all tempering temperatures, the calculated values of P_{GY} are higher than P_{max} from the load–deflection curves. Therefore, the crack initiation in Charpy specimens occurs before reaching the general yield. It should be noted also that P_{max} increases with increasing tempering temperatures, while S_y decreases with increasing tempering temperatures. This phenomenon can be explained by the local amplification of stress in the vicinity of the notch. The applied load increases while local stress in the notch root reaches critical stresses for microvoid formation. When the notched specimen is loaded elastically, the stress near the notch may locally exceed the yield stress of the material, and plastic deformation starts to occur. As result, the radius of the notch increases and the stress concentration decreases. The local plastic deformation delays the crack initiation stage and the specimen can be loaded up to macroscopic yields. It should be noted that the critical stresses for microvoid formation have been shown to be the same in steels with different carbon content, while UTS decreased with the decrease in carbon content [7]. In UHS steels, plastic deformations are restricted; therefore, critical stresses for microvoid formation are attained much earlier than in steels with low UTS, and cracks initiate during the elastic stage of loading. The plasticity increases and YS decreases after tempering at high temperatures relative to tempering at low temperatures; thus, stress concentrations near the notch decrease due to local plastic deformation, and crack initiation occurs at higher loads.

After crack initiation, a decline in the elastic region on the load–deflection curves is observed (Figure 4). The load reaches P_{max} and then slowly decreases until the final separation of the specimen into two pieces. No indications of a sharp decrease in the load after the crack initiation stage were found.

Table 2. The P_{max} from Charpy load–deflection curves and calculated P_{GY} for the 0.4%C-1.6%Si-1%Cr-0.95%Mo steel with V and Nb after quenching from 900 °C into water and tempering at different temperatures.

Tempering Temperature, °C	20	200	280	400	500	600	650
P_{max}, kN	13.5	16.9	17.7	16.8	25.3	27.8	29.5
P_{GY}, kN	33.8	38.1	39.7	39.6	33.1	34.2	30.7

Therefore, the crack propagates by a stable mechanism [28]. Almost all absorbed energy corresponds to the crack propagation stage of fractures because the crack is initiated in the elastic region where energy consumption is low.

3.4. Microstructure after Quenching

The microstructure after quenching is shown in Figure 5 and structural characteristics are summarized in Table 3. Microstructural analyses reveal typical a hierarchical sequence of structural elements of lath martensite, i.e., PAGs, packets, blocks, and laths [4]. The average PAG size revealed by reconstructions from the EBSD map is 12.2 μm (Figure 5a), and the average distance between clearly visible high-angle boundaries is 0.84 μm (Figure 5b).

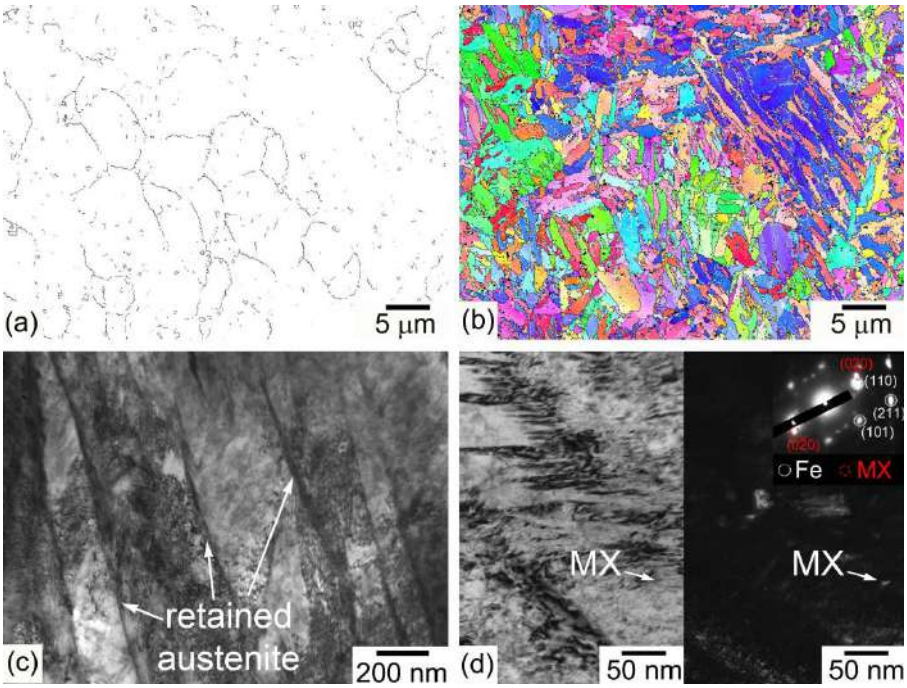

Figure 5. Typical microstructure of the 0.4%C-1.6%Si-1%Cr-0.95%Mo steel with V and Nb after water quenching: the reconstruction of prior austenite grains from an EBSD map (**a**) and EBSD map with martensite packets and blocks. The white and black lines on OIM micrographs mean boundaries with misorientations below and above 15 deg, respectively (**b**). TEM micrograph of martensite lath structure (**c**). TEM micrograph of Nb(C,N) carbonitride within the lath (bright field on the left and dark field on the right side) (**d**).

The transverse lath size is 137 nm and the dislocation density within laths is 1.5×10^{15} m^{-2} (Figure 5c). The small quantity of retained austenite is revealed between laths (Figure 5c). The nanoscale particles of MX carbonitrides with a size of ~9 nm are observed within laths (Figure 5d). It should be noted that coarse carbonitrides with a size of ~60 nm are also revealed in the microstructure. The average size of MX carbonitrides is 40 nm (Table 3). It is apparent that these dispersoids precipitate in austenite and effectively pin grain boundaries during austenitizing processes, which results in small-sized PAGs.

Table 3. Microstructural parameters of the 0.4%C-1.6%Si-1%Cr-0.95%Mo steel with V and Nb after quenching from 900 °C into water and tempering at different temperatures.

Tempering Temperature, °C	20	280	400	500	600
PAG size, μm	12.2 ± 0.7	–	–	–	–
Distance between HAB, μm	0.84 ± 0.03	–	–	–	–
Lath size, nm	137 ± 10	152 ± 31	203 ± 20	210 ± 14	200 ± 12
Dislocation density, 10^{14} m^{-2}	15 ± 2	8.6 ± 1.6	5.1 ± 1.1	5.8 ± 1.0	5.9 ± 1.3
Cementite size, nm	–	5/17	15/125	–	–
ε-carbide size (width/length), nm	–	(6 ± 1)/(31 ± 10)	(7 ± 1)/(52 ± 10)	–	–
Carbonitrides size, nm	40 ± 11	40 ± 10	41 ± 10	43 ± 11	46 ± 5
$M_{23}C_6$, nm	–	–	–	35 ± 9	49 ± 17
M_6C, nm	209 ± 16	210 ± 16	207 ± 20	211 ± 12	208 ± 7

The high strength of the steel after water quenching correlates with the revealed microstructure. An extremely high dislocation density and small martensitic laths thicknesses provide strong strengthening by dislocations and laths boundaries. Most of the carbon is retained in solid solution after water quenching and increases strength. The dispersion particles of M_6C carbides and MX precipitates provide dispersion hardening. The most effective strengthening mechanisms after water quenching are solid solution strengthening, strengthening by dislocations and grain boundaries. The dispersion strengthening is less effective because of the low volume fraction of MX carbonitrides and coarse size of M_6C carbides.

3.5. Microstructure after Tempering Treatments

Tempering results in decreased lattice dislocation densities and increased lath thicknesses. No effect of tempering on the dimension of PAGs, packet, and distance between the high-angle boundaries is found. After tempering at 200 °C, two types of particles are revealed (Figure 6). The first type comprises MX carbonitrides, which contain 51% of Nb. Thermo-Calc predicts a similar composition of the particles within the temperature region of 900–1000 °C (Figure 1). The average size of the MX carbonitrides remains virtually unchanged (Table 3). The second type of precipitate is M_6C carbides with an average size of 120 nm. These carbides are enriched by Mo (Figure 6). Thermo-Calc calculations predict the precipitation of M_6C carbides at temperatures from 400 to 900 °C (Figure 1a). It seems that both MX carbonitrides and M_6C carbides precipitate during solution treatments and are retained after tempering processes. It should be noted that neither ε-carbide nor M_3C carbides are found after tempering at 200 °C, probably due to alloying with Si, which delays the precipitation of carbides [22].

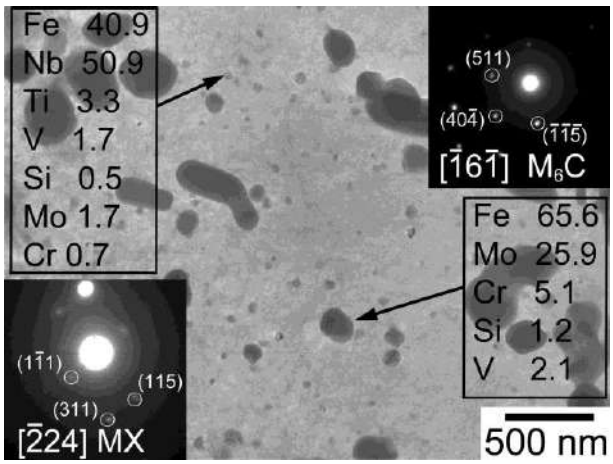

Figure 6. Typical precipitates in the thin foil of the 0.4%C-1.6%Si-1%Cr-0.95%Mo steel with V and Nb after quenching and tempering at 200 °C.

Tempering at 280 °C leads to a 40% decrease in lattice dislocation densities and 10% increase in lath thicknesses (Table 3, Figure 7a). The same MX carbonitrides enriched with Nb after tempering at 200°C are revealed in the microstructure (Figure 7b). The precipitation of ε-carbide with strip-like shapes and needle-like cementite particles, concurrently, is observed (Figure 7c,d). However, only a few cementite particles are found (Figure 7d). The ε-carbide is dominant among all secondary phase particles after tempering at 280 °C.

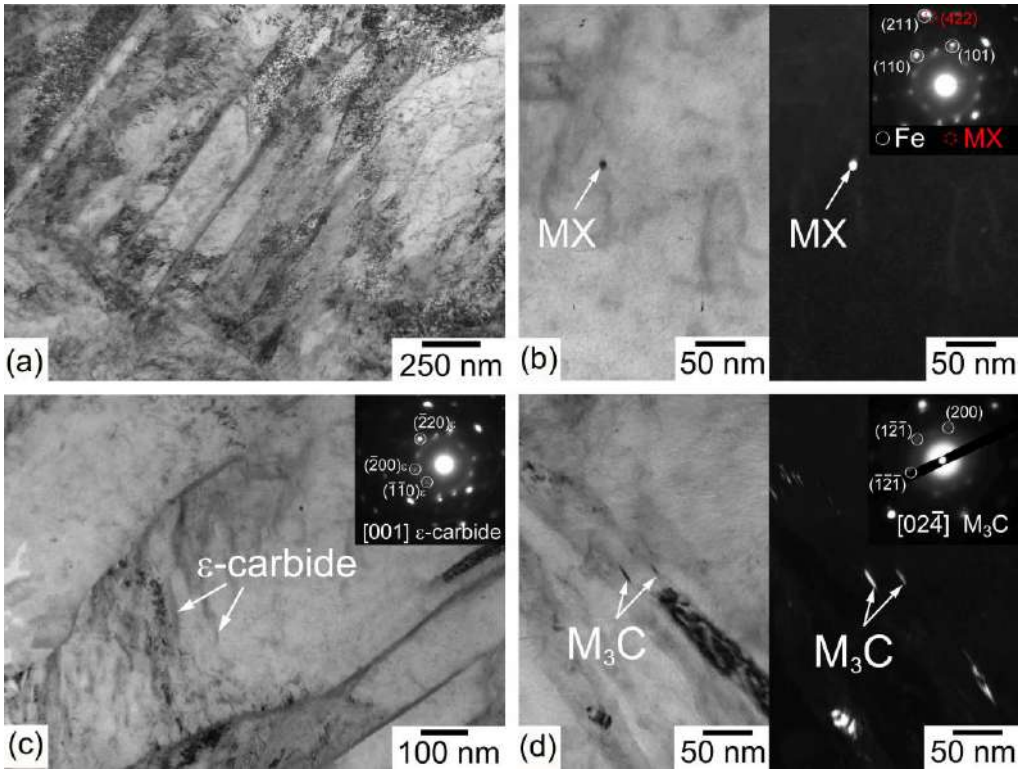

Figure 7. Typical microstructure of the 0.4%C-1.6%Si-1%Cr-0.95%Mo steel with V and Nb after quenching and tempering at 280 °C: TEM micrograph of martensite lath structure (**a**); TEM micrograph of Nb(C,N) carbonitride within the lath (**b**); TEM micrograph of ε-carbide within the lath (**c**); TEM micrograph of cementite within the lath (**d**).

The results of microstructure investigation may explain the maximum on the DSC curve (Figure 2) at a temperature of 280 °C. Obviously, this maximum appears due to precipitation of ε-carbide with strip-like shapes because no precipitation of other phases with significant volume fractions is revealed experimentally.

The laths size and dislocation density of the steel scarcely change after tempering at 280 °C. Therefore, a high value of strengthening by dislocations and laths boundaries is retained in the tempered steel. The precipitation of ε-carbides leads to the depletion of solid solution by carbon and reduction in solid solution strengthening; as a consequence, the UTS of the steel decreases (Table 3). However, additional particles of ε-carbides increase dispersion strengthening of the steel and YS increases in comparison with water-quenched steel.

The tempering at a temperature of 400 °C leads to a decrease in the lattice dislocation density by a factor of 3 and an increase in the lath thickness by 30% in comparison with the quenched specimen (Table 3, Figure 8a). The phase composition of the steel is retained as the same after tempering at 280 °C. MX carbonitrides, ε-carbide, and M_3C carbides are cohabitated in the microstructure (Figure 8). The lengthening of the ε-carbide takes place with increasing tempering temperatures from 280 to 400 °C, and this increases the diameter-to-thickness aspect ratio (AR) from 5 to 7 (Table 3).

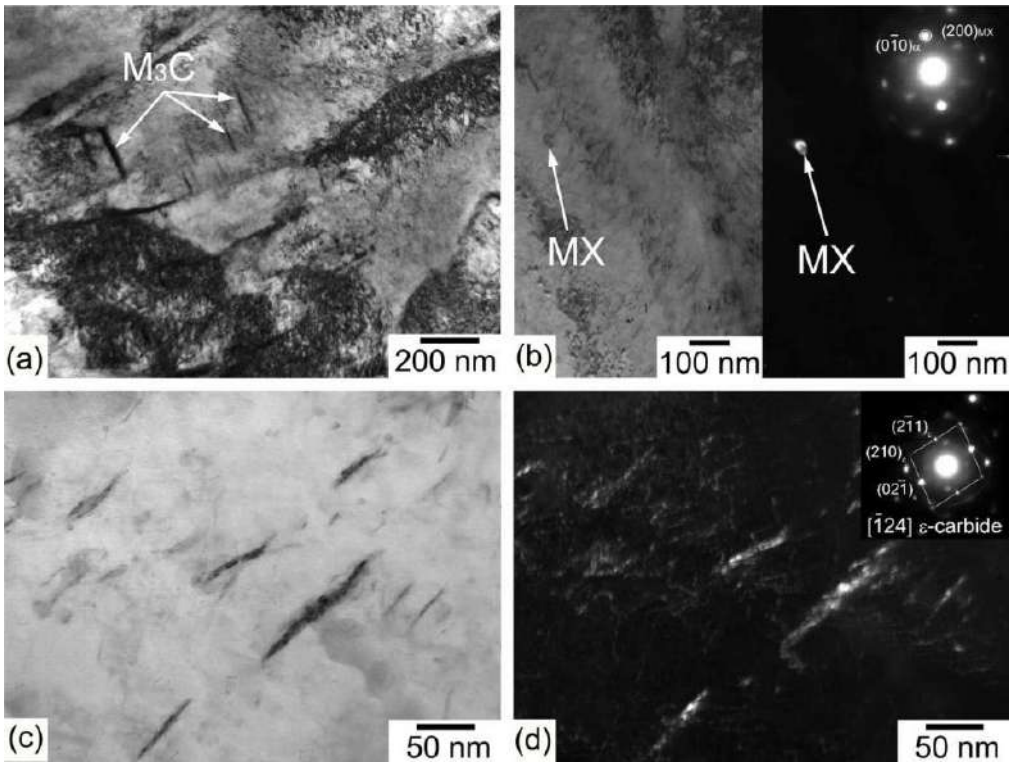

Figure 8. Typical microstructure of the steel after quenching and tempering at 400 °C: TEM micrograph of martensite lath structure with cementite particles (**a**); TEM micrograph of Nb(C,N) carbonitride within the lath (bright field on the left and dark field on the right side) (**b**); TEM micrograph of ε-carbide within the lath (bright field) (**c**); TEM micrograph of ε-carbide within the lath (dark field) (**d**).

Almost no growth in the ε-carbide in the transverse direction is found and ε-carbides exhibit well-defined rod shapes [9]. The AR of cementite increases from 3 to 8 (Table 3). In general, the coherency of longitudinal interfaces is responsible for the lengthening of particles [29].

The ε-carbide typically dissolves between 300 and 350 °C [9]. However, in the present steel, this carbide is retained up to a tempering temperature of 400 °C, and this can be attributed with its high-silicon content [30]. The solubility of silicon in cementite is negligible and strong enrichment areas with a thickness of 1–2 nm around the cementite appear [9]; these cease the growth of cementite particles. This process has to occur in order to provide the dissolution of ε-carbides as metastable phases in accordance with the well-known Gibbs–Thomson schema, taking into account that ε-carbide and cementite nucleate independently [9,29]. In contrast, no significant enrichment by Si takes place within the vicinity of ε-carbides [9]. However, in the present steel, the extensive coarsening of cementite takes place and accompanies no dissolution of ε-carbides (Figures 7 and 8, Table 3).

The strengthening by dislocations and laths boundaries decrease after tempering at 400 °C in comparison with water-quenched steel due to the decrease in dislocations density and increase in laths thickness. However, the particles size (Table 3) and their mass portion (Figure 1a) remain the same as after tempering at 280 °C; as a result, the YS and UTS scarcely change.

The increase in tempering temperature from 500 to 600 °C affects lattice dislocation densities and lath thickness insignificantly (Table 3, Figure 9a,d). At 500 °C, the $M_{23}C_6$ carbides with nearly round shapes and an average size of ~35 nm precipitate (Figure 9b).

No particles of cementite and/or ε-carbide are found. Therefore, the following precipitation sequence take place in the present steel:

$$\varepsilon\text{-carbide} + M_3C \rightarrow M_{23}C_6 \quad (1)$$

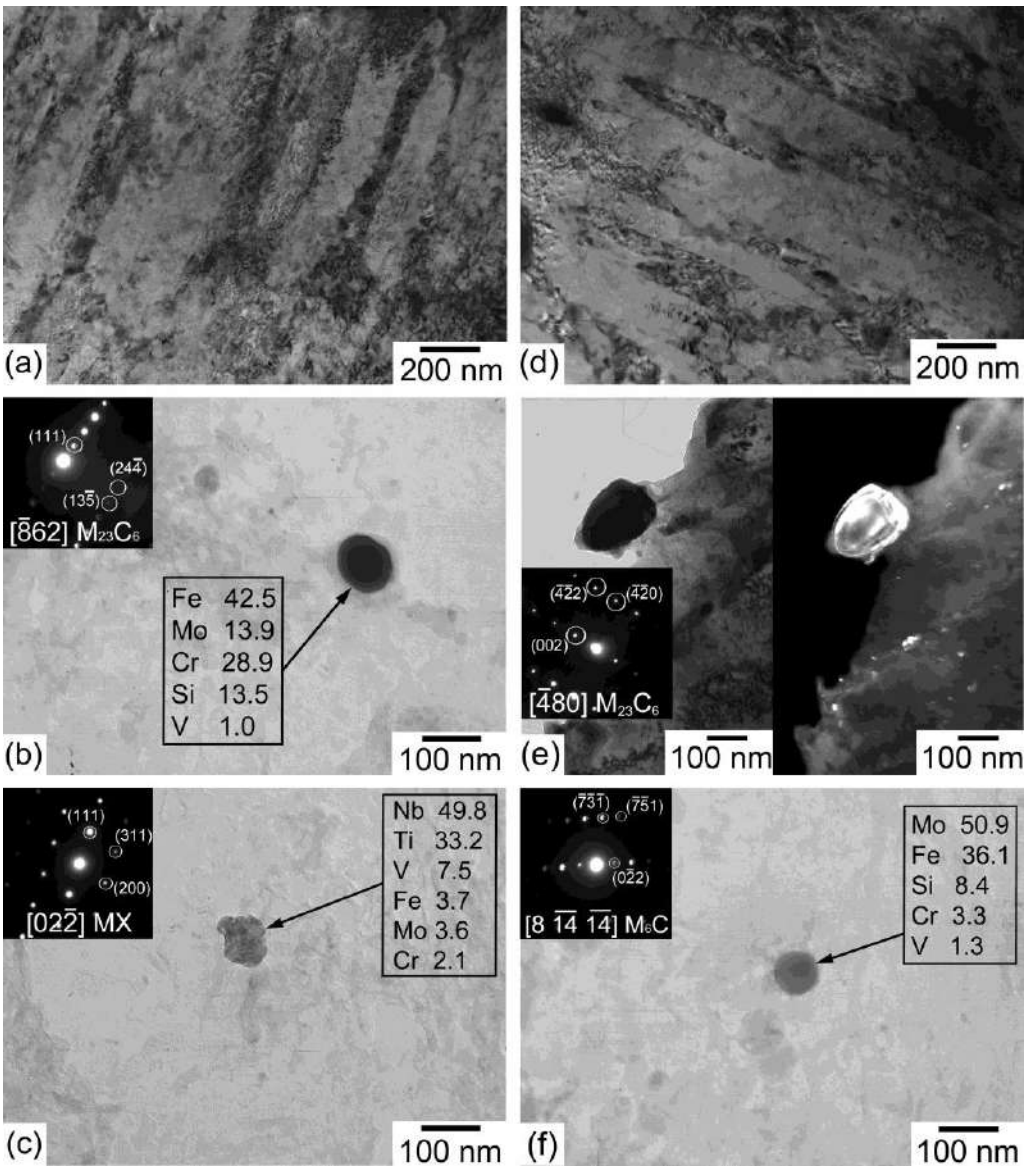

Figure 9. Typical microstructures of the steel after quenching and tempering at 500 °C (**a**–**c**) and 600 °C (**d**–**f**): TEM micrograph of martensite lath structure with carbide particles at 500 °C (**a**) and 600 °C (**d**); TEM micrograph of $M_{23}C_6$ carbide on carbon replica after tempering at 500 °C (**b**) and on thin foil after tempering at 600 °C in bright (left side) and dark (right side) field (**e**); MX precipitates on carbon replica after tempering at 500 °C (**c**) and M_6C carbide on carbon replica after tempering at 600 °C (**f**).

Carbides in precipitation sequence (1) co-exist with MX and M_6C carbides (Figure 9, Table 3), which is correlated with the literature data [31].

Further increases in tempering temperatures from 600 to 650 °C scarcely affect the phase composition of the steel, and the same precipitates after tempering at 500 °C are observed (Figure 9e,f, Table 3). However, the larger secondary precipitates lead to a decrease in the tensile strength and hardness of the steel.

An inspection of experimental results shows that an increase in YS is attributed to the precipitation of nanosized ε-carbide; carbon depletion from martensite strongly decreases the value of solid solution strengthening and an increase in lath thickness decreases the contribution of grain-boundary strengthening. Therefore, dispersion strengthening attributed to the precipitation of ε-carbide plays a vital role in the YS of the present steel tempered in the temperature range of 280–400 °C.

The additions of Si, Mo, and Cr hinder the dissolution of ε-carbides after the precipitation of cementite. The origin of this phenomenon is unclear. It is worth noting that the precipitation of $M_{23}C_6$ occurs on high- and low-angle boundaries of the lath martensite structure (Figure 9e) [10,32]; therefore, at T ≥ 467 °C, tempering leads to the replacement of matrix ε-carbide and cementite particles contributing to dispersion strengthening by boundary $M_{23}C_6$ carbides. Only $M_{23}C_6$ carbides located on the lath and block boundaries may contribute to dispersion strengthening [33]. The change in the dispersion of strengthening particles results in a significant decrease in the YS of the studied steel (Table 1).

3.6. Fractography

The low- and high-magnification SEM images of the fracture surfaces of Charpy impact specimens after tempering at 280 °C and 500 °C are shown in Figure 10. The results of the fractography study support the data obtained from an instrumented Charpy V-notch test. The ductile crack extension is revealed both after low tempering and high tempering temperatures. The fracture surfaces consist of dimples and a small fraction of cleavage facets.

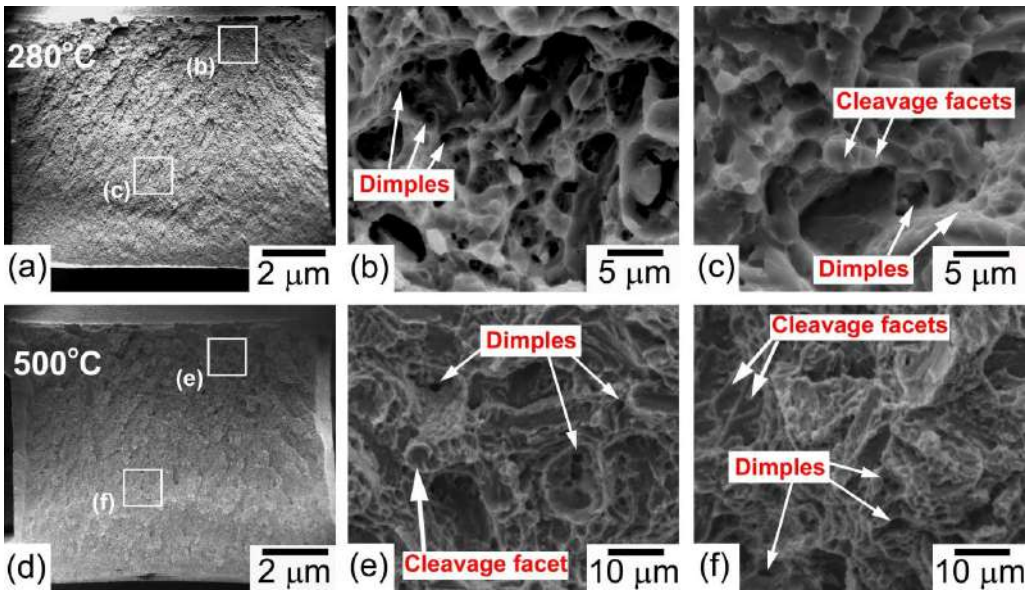

Figure 10. Fracture surfaces of the Charpy V-notch specimens after tempering at 280 °C (**a**–**c**) and 500 °C (**d**–**f**) tested at 20 °C: general view (**a**,**d**) and high magnification of the portions indicated by frames (**b**,**c**,**e**,**f**).

Usually, high-carbon steels including an AISI4340 steel with 0.4%C after austenitizing followed by water quenching and tempering up to 400 °C show transgranular cleavage fractures [7]. The cleavage originates from interlath cementite crystals, which precipitate during tempering due to the decomposition of retained austenite [22]. However, in contrast with the AISI4340 steel, the studied steel contains 1.6% Si, which slows down the kinetics of cementite precipitation in the retained austenite [7,22], and only a few particles of cementite are revealed after tempering at temperatures of 280–400 °C. As a result, no interlath cleavage occurs.

At low tempering temperatures within 280–400 °C, the major precipitation in the studied steel is ε-carbide, which is homogeneously distributed through the microstructure.

These particles provide high tensile strength and hardness (Table 1). However, the Charpy impact toughness is revealed to be low. It is well known that the high rates of strain hardening in high-carbon steels reduce the amount of plastic deformation required to reach the critical fracture stress at the notch root in Charpy specimen [7]. Therefore, the formation of a magistral crack occurs in the elastic region before attaining the general yielding of the specimen. The high density of ε-carbide particles serves as microcrack initiation locations in front of the propagating macrocrack with critical dimension. Local plastic deformations at the tips of the microcracks lead to the formation of voids, which coalesce and form dimpled fracture surfaces. The absence of general yielding and the high rate of strain hardening result in a low possibility of absorbing the impact energy and, thus, low-impact toughness is observed.

At high tempering temperatures within 500–650 °C, the precipitation of carbides in accordance with precipitation sequence (1) and the growth of MX carbides provide an increase in the volume fraction of precipitated carbides (Figure 1a) and the depletion of carbon from martensite. The rate of strain hardening decreases, and local plastic deformations reaching critical fracture stresses at the notch root increase. The macrocrack with critical dimensions still nucleates before general yields, but higher macroscopic loads are required for its propagation in comparison with steel after tempering at 200–400 °C (Figure 4).

4. Conclusions

The effect of tempering on the microstructure and mechanical properties of the steel Fe-0.43C-1.60Si-0.01Mn-1.1Cr-0.95Mo-0.08V-0.05Nb-0.04Ti-0.003B-0.007S-0.004P is studied. The results can be summarized as follows:

1. Quenching produces a high dislocation density of 1.5×10^{15} m^{-2} and a small lath thickness of 137 nm. Tempering in the temperature range of 200–600 °C decreases the density of free dislocations and increases the lath thicknesses insignificantly to 5.4×10^{14} m^{-2} and 210 nm, respectively.

2. The precipitation sequence of

$$\varepsilon\text{-carbide} + M_3C \rightarrow M_{23}C_6$$

takes place. The additions of Si, Cr, and Mo result in a shift in the precipitation temperatures of ε-carbides and cementite toward high temperatures and provide the co-existence of ε-carbide and cementite after 1 h tempering in the temperature interval of 280–400 °C. The precipitation of boundary $M_{23}C_6$ carbides leads to a full dissolution of ε-carbide and cementite. The growth of MX carbides from 40 to 45 nm precipitated from martensite occurs during tempering.

3. The high strengthening after tempering within a temperature range of 280–400 °C originates from the precipitation of ε-carbides. The yield stress increases from 1445 MPa in the quenched condition to 1625 MPa after tempering at 200 °C and then slowly increases to 1690 MPa, while the tempering temperature increases to 400 °C. The ultimate tensile strength gradually decreases from 2120 to 1930 MPa while the tempering temperature increases from 200 to 400 °C. A noticeable decrease in strength occurs after tempering at 500 °C, when yield stresses decrease toward 1415 MPa and the ultimate tensile strength decreases toward 1680 MPa.

4. The Charpy V-notch impact-absorbed energy of 12–14 J/cm^2 is revealed after tempering within the temperature range of 200–400 °C. The increase in tempering temperatures from 500 to 650 °C leads to a gradual increase in impact-absorbed energy from 20 to 33 J/cm^2.

Author Contributions: Conceptualization, V.D. and R.K.; methodology, V.D. and D.Y.; validation, D.Y., S.G. and S.V.; formal analysis, D.Y.; investigation, V.D., D.Y., S.G., S.V. and R.K.; resources, R.K.; data curation, D.Y. and V.D.; writing—original draft preparation, V.D. and R.K.; writing—review and editing, D.Y.; visualization, D.Y.; supervision, R.K.; project administration, R.K.; funding acquisition, R.K. All authors have read and agreed to the published version of the manuscript.

Funding: This research was funded by the Ministry of Science and Higher Education of the Russian Federation, grant number 075-15-2021-572.

Data Availability Statement: Not applicable.

Acknowledgments: The studies were carried out on the equipment of the Joint Scientific Center for Technologies and Materials of Belgorod State National Research University, which was supported by the Ministry of Science and Higher Education of the Russian Federation under contract No. 075-15-2021-690 (unique identifier RF—-2296.61321X0030).

Conflicts of Interest: The authors declare no conflict of interest.

References

1. Tomita, Y. Development of fracture toughness of ultrahigh strength, medium carbon, low alloy steels for aerospace applications. *Int. Mater. Rev.* **2000**, *45*, 27–37. [CrossRef]
2. Youngblood, J.L.; Raghavan, M. *Microstructure and Mechanical Properties of Quenched and Tempered 300M Steel*; National Aeronautics and Space Administration, Scientific and Technical Information Office: Washington, DC, USA, 1978.
3. *Military Handbook—MIL-HDBK-5H: Metallic Materials and Elements for Aerospace Vehicle Structures*; The Department of Defense: Washington, DC, USA, 2003.
4. Kitahara, H.; Ueji, R.; Tsuji, N.; Minamino, Y. Crystallographic features of lath martensite in low-carbon steel. *Acta Mater.* **2006**, *54*, 1279–1288. [CrossRef]
5. Dolzhenko, A.; Pydrin, A.; Gaidar, S.; Kaibyshev, R.; Belyakov, A. Microstructure and Strengthening Mechanisms in an HSLA Steel Subjected to Tempforming. *Metals* **2021**, *12*, 48. [CrossRef]
6. Xiong, Z.; Timokhina, I.; Pereloma, E. Clustering, nano-scale precipitation and strengthening of steels. *Prog. Mater. Sci.* **2020**, *118*, 100764. [CrossRef]
7. Krauss, G. *Steels: Processing Structure, and Performance*, 2nd ed.; ASM International: Materials Park, OH, USA, 2005.
8. Kim, B.; Celada, C.; Martín, D.S.; Sourmail, T.; Rivera-Díaz-Del-Castillo, P. The effect of silicon on the nanoprecipitation of cementite. *Acta Mater.* **2013**, *61*, 6983–6992. [CrossRef]
9. Forsik, S.A.; Rivera-Diaz-Del-Castillo, P.E. Martensitic Steels: Epsilon Carbides in Tempered. In *Encyclopedia of Iron, Steel, and Their Alloys*; Taylor and Francis: New York, USA, 2016; pp. 2169–2181. [CrossRef]
10. Fedoseeva, A.; Dudova, N.; Kaibyshev, R. Creep strength breakdown and microstructure evolution in a 3%Co modified P92 steel. *Mater. Sci. Eng. A* **2015**, *654*, 1–12. [CrossRef]
11. Vervynckt, S.; Verbeken, K.; Lopez, B.; Jonas, J.J. Modern HSLA steels and role of non-recrystallisation temperature. *Int. Mater. Rev.* **2012**, *57*, 187–207. [CrossRef]
12. Hidalgo, J.; Santofimia, M.J. Effect of Prior Austenite Grain Size Refinement by Thermal Cycling on the Microstructural Features of As-Quenched Lath Martensite. *Met. Mater. Trans. A* **2016**, *47*, 5288–5301. [CrossRef]
13. Galindo-Nava, E.; Rivera-Díaz-Del-Castillo, P. A model for the microstructure behaviour and strength evolution in lath martensite. *Acta Mater.* **2015**, *98*, 81–93. [CrossRef]
14. Dong, J.; Zhou, X.; Liu, Y.; Li, C.; Liu, C.; Guo, Q. Carbide precipitation in Nb-V-Ti microalloyed ultra-high strength steel during tempering. *Mater. Sci. Eng. A* **2016**, *683*, 215–226. [CrossRef]
15. Yan, Z.; Liu, K.; Eckert, J. Effect of tempering and deep cryogenic treatment on microstructure and mechanical properties of Cr–Mo–V–Ni steel. *Mater. Sci. Eng. A* **2020**, *787*, 139520. [CrossRef]
16. Ren, J.; Li, C.; Han, Y.; Li, E.; Gao, C.; Qiu, C. Effect of initial martensite and tempered carbide on mechanical properties of 3Cr2MnNiMo mold steel. *Mater. Sci. Eng. A* **2021**, *812*, 141080. [CrossRef]
17. *ASTM E 23-12c*; Standard Test Methods for Notched Bar Impact Testing of Metallic Materials. ASTM International: West Conshohocken, PA, USA, 2013; pp. 1–25. [CrossRef]
18. Gey, N.; Humbert, M. Characterization of the Variant Selection Occurring during the A→β→α Phase Transformations of a Cold Rolled Titanium Sheet. *Acta Mater.* **2002**, *50*, 277–287. [CrossRef]
19. Hua, P.; Mironov, S.; Sato, Y.S.; Kokawa, H.; Park, S.H.C.; Hirano, S. Crystallography of Martensite in Friction-Stir-Welded 12Cr Heat-Resistant Steel. *Met. Mater. Trans. A* **2019**, *50*, 3158–3163. [CrossRef]
20. Dudko, V.; Fedoseeva, A.; Kaibyshev, R. Ductile-brittle transition in a 9% Cr heat-resistant steel. *Mater. Sci. Eng. A* **2016**, *682*, 73–84. [CrossRef]
21. Dolzhenko, A.; Yanushkevich, Z.; Nikulin, S.; Belyakov, A.; Kaibyshev, R. Impact toughness of an S700MC-type steel: Tempforming vs ausforming. *Mater. Sci. Eng. A* **2018**, *723*, 259–268. [CrossRef]
22. Horn, R.M.; Ritchie, R.O. Mechanisms of tempered martensite embrittlement in low alloy steels. *Met. Mater. Trans. A* **1978**, *9*, 1039–1053. [CrossRef]
23. Antolovich, S.D.; Armstrong, R.W. Plastic strain localization in metals: Origins and consequences. *Prog. Mater. Sci.* **2014**, *59*, 1–160. [CrossRef]
24. Kimura, Y.; Inoue, T. Mechanical Property of Ultrafine Elongated Grain Structure Steel Processed by Warm Tempforming and Its Application to Ultra-High-Strength Bolt. *ISIJ Int.* **2020**, *60*, 1108–1126. [CrossRef]

25. Kimura, Y.; Inoue, T. Influence of Carbon Content on Toughening in Ultrafine Elongated Grain Structure Steels. *ISIJ Int.* **2015**, *55*, 1135–1144. [CrossRef]
26. Server, W.L. General Yielding of Charpy V-Notch and Precracked Charpy Specimens. *J. Eng. Mater. Technol.* **1978**, *100*, 183–188. [CrossRef]
27. Knott, J.F. *Fundamentals of Fracture Mechanics*; The Butterworth Group: London, UK, 1973.
28. Chaouadi, R.; Fabry, A. On the Utilization of the Instrumented Charpy Impact Test for Characterizing the Flow and Fracture Behawiour of Reactor Pressure Vessel Steel. In *From Charpy to Present Impact Testing*; Franqois, D., Pineau, A., Eds.; Elsevier Science Ltd. and ESIS: Oxford, UK, 2002; pp. 103–117. ISBN 9780080528977.
29. Porter, D.A.; Esterling, K.E.; Sherif, M. *Phase Transformation in Metals and Alloys*, 3rd ed.; CRS Press: Boca Raton, FL, USA, 2009.
30. Kozeschnik, E.; Bhadeshia, H.K.D.H. Influence of silicon on cementite precipitation in steels. *Mater. Sci. Technol.* **2008**, *24*, 343–347. [CrossRef]
31. Fedoseeva, A.; Dudova, N.; Glatzel, U.; Kaibyshev, R. Effect of W on tempering behaviour of a 3%Co modified P92 steel. *J. Mater. Sci.* **2016**, *51*, 9424–9439. [CrossRef]
32. Fedorova, I.; Kostka, A.; Tkachev, E.; Belyakov, A.; Kaibyshev, R. Tempering behavior of a low nitrogen boron-added 9%Cr steel. *Mater. Sci. Eng. A* **2016**, *662*, 443–455. [CrossRef]
33. Tkachev, E.; Belyakov, A.; Kaibyshev, R. Creep behavior and microstructural evolution of a 9%Cr steel with high B and low N contents. *Mater. Sci. Eng. A* **2018**, *725*, 228–241. [CrossRef]